

Efficient postacquisition synchronization of 4-D nongated cardiac images obtained from optical coherence tomography: application to 4-D reconstruction of the chick embryonic heart

Aiping Liu

Ruikang Wang

Oregon Health & Science University
School of Medicine
Division of Biomedical Engineering
3303 SW Bond Ave.
Mail Code CH13B
Portland, Oregon 97239

Kent L. Thornburg

Oregon Health & Science University
Heart Research Center
3303 SW Bond Ave.
Mail Code: CH15H
Portland, Oregon 97239

Sandra Rugonyi

Oregon Health & Science University
School of Medicine
Division of Biomedical Engineering
3303 SW Bond Ave.
Mail Code CH13B
Portland, Oregon 97239

Abstract. Four-dimensional (4-D) imaging of the embryonic heart allows study of cardiac morphology and function *in vivo* during development. However, 4-D imaging of the embryonic heart using current techniques, including optical coherence tomography (OCT), is limited by the rate of image acquisition. Here, we present a nongated 4-D imaging strategy combined with an efficient postacquisition synchronization procedure that circumvents limitations on acquisition rate. The 4-D imaging strategy acquires a time series of images in B mode at several different locations along the heart, rendering out-of-phase image sequences. Then, our synchronization procedure uses similarity of local structures to find the phase shift between neighboring image sequences, employing M-mode images (extracted from the acquired B-mode images) to achieve computational efficiency. Furthermore, our procedure corrects the phase shifts by considering the phase lags introduced by peristaltic-like contractions of the embryonic heart wall. We applied the 4-D imaging strategy and synchronization procedure to reconstruct the cardiac outflow tract (OFT) of a chick embryo, imaged with OCT at early stages of development (Hamburger–Hamilton stage 18). We showed that the proposed synchronization procedure achieves efficiency without sacrificing accuracy and that the reconstructed 4-D images properly captured the dynamics of the OFT wall motion. © 2009 Society of Photo-Optical Instrumentation Engineers. [DOI: 10.1117/1.3184462]

Keywords: cardiac development; chick embryonic heart; outflow tract; cardiac imaging; cardiac reconstruction; postacquisition synchronization; M-mode image; phase lag.

Paper 09054R received Feb. 17, 2009; revised manuscript received Jun. 1, 2009; accepted for publication Jun. 3, 2009; published online Jul. 31, 2009.

1 Introduction

During embryonic development, the heart undergoes a complex morphogenetic process that forms a primitive beating tubular heart, which ultimately becomes a four-chambered heart.^{1,2} Cardiac structure and function interact during this process to ensure normal cardiac development,³ and disturbances can lead to congenital heart defects (e.g., Ref. 4–6). Four-dimensional (4-D) imaging [imaging of three-dimensional (3-D) structures over time] of the embryonic heart at early stages of development, when the heart is an unseptated tube, is challenging due to the small dimensions of the heart [e.g., typically <2 mm Ref. 7] and the rapid cardiac motion (typically, more than two heartbeats per second⁸).

Optical coherence tomography (OCT) is a powerful imaging technique that can be applied to the visualization and quantification of morphological and functional properties of

the heart during development. The technique offers high-resolution, noninvasive imaging of microstructures up to a depth of ~2–3 mm in biological tissues.^{9–12} Compared to other non-invasive imaging modalities, such as confocal microscopy^{13,14} and high-frequency ultrasound,¹⁵ OCT combines the high-resolution (at micrometer scale) capabilities of confocal microscopy with the large depth of field in tissue (at millimeter scale) of ultrasound. Thus OCT is especially suitable for imaging the embryonic heart at early developmental stages.^{16–18} OCT has been used to image the embryonic hearts of frog,^{19,20} chick,^{16,18,21,22} and mouse.^{16,23}

OCT has been applied to 4-D imaging of *Xenopus laevis* and quail embryonic hearts,^{20,24} however, the current rate of image acquisition (up to 20 cardiac volumes per second) is not fast enough to study the dynamics of the beating embryonic hearts.²⁴ To circumvent limitations in the image acquisition rate, 4-D cardiac images can be reconstructed by postprocessing two-dimensional (2-D) image sequences (B-mode

Address all correspondence to: Sandra Rugonyi, Oregon Health & Science University, School of Medicine, Division of Biomedical Engineering, Mail Code CH13B, Portland, Oregon 97239; E-mail: rugonyis@ohsu.edu

images) that together span the entire heart. This 4-D cardiac imaging procedure requires synchronization of B-mode images to enable proper reconstruction of the 3-D geometry of the heart at sequential phases (time points) over the cardiac cycle. To synchronize 2-D image sequences, two approaches have been used:²⁵ (i) the prospective-gated (or hardware-gated) approach, in which acquisition of image sequences is triggered at a particular (known) phase of the cardiac cycle by a cardiac signal, and therefore, the acquired image sequences are synchronized (in phase), and (ii) the retrospective-gated (or nongated) approach, in which acquisition of image sequences is not triggered; hence, image sequences start at random phases of the cardiac cycle and image postprocessing is required to synchronize them. Jenkins et al.²⁶ performed prospective-gated OCT imaging of the heart of an early developing chick embryo, triggering image acquisition with signals obtained by a laser Doppler velocimeter from a vitelline vessel. Mariampillai et al.²⁷ performed retrospective-gated OCT imaging of a chick embryonic heart using Doppler velocities: during acquisition of B-mode structural images of the chick heart, they simultaneously collected Doppler signals from an aortic arch with a separate Doppler OCT system. Then, Doppler data were used to synchronize B-mode image sequences. The advantage of Mariampillai's imaging strategy was that imaging and image reconstruction were uncoupled. However, as with the prospective gated strategy, cardiac gating signals were needed to provide time stamps for postacquisition synchronization. Therefore, errors introduced by weak gating signals—often encountered in the embryonic developing heart—affected the accuracy of 4-D reconstruction. To eliminate the need of additional cardiac signals, Liebling et al.^{28,29} developed a retrospective-gated imaging strategy and image reconstruction procedure, and applied them to 4-D imaging of the zebra-fish heart. In their approach, nongated B-mode images of the zebra fish heart were acquired using confocal microscopy at different depths, spanning the whole heart. Then, B-mode images were synchronized by invoking structural similarity between adjacent image sequences. To achieve computational efficiency of the synchronization algorithms, Liebling et al.^{28,29} used a subset of the wavelet series representation of the images for data reduction.

In this paper, we present an alternative nongated 4-D imaging strategy combined with a simple and efficient postacquisition synchronization procedure to reconstruct 4-D images of the *in vivo* embryonic heart. B-mode images of transverse sections of the heart are acquired without gating. To achieve computational efficiency, our postacquisition synchronization procedure uses M-mode images (line scans over time),³⁰ extracted from the B-mode images; synchronization of adjacent image sequences is then achieved by applying structural similarity along a line. In our procedure, we found that synchronization of image data based on similarity of local structures alone does not fully recover the peristaltic-like motion of the embryonic heart wall, which introduces phase lags in cardiac wall motion. Our synchronization procedure accounts for this phase lag by adjusting the phase of each image sequence after synchronization based on structural similarity was performed.

We applied the nongated 4-D imaging strategy and post-processing synchronization procedure to OCT images of the cardiac outflow tract (OFT) of a chick embryo. We studied the chick embryo because at early stages, cardiac development in

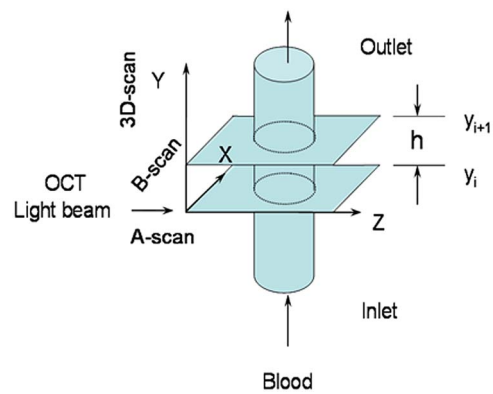


Fig. 1 Schematic representation of nongated 4-D image acquisition strategy.

the chicken is similar to that in humans;¹ the chick embryonic heart is also easy to access and develops faster than most other animal models.³¹ OCT images of the OFT were acquired *in vivo* at an early developmental stage, Hamburger–Hamilton (HH) 18 (~3 days of incubation).³² At this early stage of development, the chick heart is tubular and has no valves; the OFT is the distal region of the embryonic heart—connecting the ventricle with the arterial system—and functions as a primitive valve by contracting to limit blood flow regurgitation. The OFT is a crucial cardiac segment to study because a large portion of congenital heart defects originate in the OFT.³³ The OFT is also a good region for testing the capability of our reconstruction procedure to capture peristaltic-like motions of the heart wall.

Section 2 of this paper presents the 4-D imaging strategy and image postacquisition synchronization procedure. Section 3 presents the application of the presented procedure to images of the chick embryonic OFT and tests of its accuracy. Finally, Sec. 4 presents a brief discussion, and Sec. 5 gives the conclusions to the paper.

2 Imaging Strategy and 4-D Image Reconstruction Procedure

2.1 Nongated 4-D Imaging Strategy

The nongated 4-D imaging strategy used (illustrated in Fig. 1) is similar to that used by Liebling et al.²⁸ B-mode image sequences are collected at successive imaging planes (X - Z planes along the Y direction in Fig. 1): starting at $y_1=0$, OCT acquires a sequence of 2-D cross-sectional images (X - Z plane) for approximately five cardiac cycles, and then the imaging plane moves longitudinally an increment h to the next cross section. Image acquisition is then repeated until the whole region of interest is spanned and y_L is reached. The value of the distance h between adjacent image planes is kept small so that structural imaging data at adjacent locations are similar. An image sequence of a longitudinal cardiac section (Y - Z plane in Fig. 1) is also acquired to adjust phase lags later. Therefore, a 4-D image data set consists of L sets of B-mode cross-sectional image sequences acquired along the Y direction and a B-mode image sequence of a longitudinal section. Because OCT image acquisition is nongated, acquired image sequences are out of phase. To reconstruct 4-D images

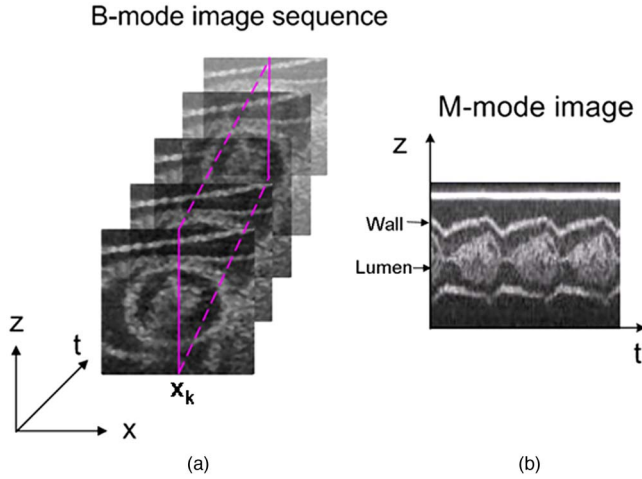


Fig. 2 Illustration of M-mode image extraction from a B-mode image sequence: (a) B-mode image sequence and (b) M-mode image extracted along a line ($x=x_k$) from (a).

of the heart, image sequences need to be synchronized; that is, the phase relationship between imaging sequences needs to be determined.

2.2 Postacquisition Synchronization Procedure

Our synchronization procedure assumes that (i) motion and deformation of the heart are periodic and (ii) changes in cardiac structural features are continuous (structural data in B-mode images acquired at adjacent locations are similar).

To synchronize the acquired image sequences, the following steps are performed:

1. determination of the cardiac period for each image sequence
2. determination of relative phase shifts between neighboring image sequences
3. determination of absolute phase shifts of image sequences relative to the first image sequence
4. estimation and adjustment of phase lags between image sequences introduced by peristaltic-like motions of the heart wall
5. synchronization of image sequences and 4-D image reconstruction.

Compared to Liebling's synchronization procedure,²⁸ our procedure has three major differences. First, to achieve computational efficiency, rather than using a subset of the image wavelet series, our synchronization procedure analyzes M-mode images that are extracted from the image sequences (see Fig. 2). Representing a B-mode image sequence at a location y_i by the intensity function $I_{y_i}(x, z, t)$, an M-mode image extracted along a vertical line $x=x_k$ of the B-mode sequence is $I'_{y_i}(z, t) = I_{y_i}(x_k, z, t)$. Second, to improve the accuracy of the synchronization procedure, instead of keeping image frames in a sequence in the order they were acquired and cropping image data to a whole number of cardiac cycles (to apply the synchronization algorithm), data from image sequences (spanning approximately five cardiac cycles) are pooled into one normalized cardiac cycle. Third, to accurately recover the dynamic motion of the heart, we provide a procedure to estimate and adjust phase lags between adjacent image

sequences introduced by peristaltic-like contractions of the heart wall. This later step may not be necessary, however, if imaging is performed at nontransversal planes of the heart (such as longitudinal planes). In Secs. 2.2.1–2.2.5, we describe each step of the synchronization procedure.

2.2.1 Determination of cardiac period

Because our synchronization procedure relies on the periodicity of the cardiac cycle, the cardiac period must be known to ensure proper synchronization of image sequences and to pool data from image sequences to a normalized cardiac cycle. To adjust for small variations in period that occur during imaging (mostly due to temperature fluctuations), we calculate the cardiac period, $T(y_i)$, of each of the L image sequences at locations y_i . To calculate $T(y_i)$, we use a string-length method (SLM).^{34,35} SLM is particularly well suited for determining periods in cases of relatively few observations (a few cycles) when conventional methods, such as the Fourier transform, fail to provide reliable results.³⁶ SLM assumes that periodic signals, discretely sampled over several cycles, are continuous. Then, if the period of the signal is known, the phase (time position within the cycle) of each data point can be determined, and “strings” (line segments) that join successive data points (arranged by their phases) have the shortest total length. Hence, the period minimizes the total length of strings.

In our implementation of the SLM algorithm, the cardiac period, T , of each image sequence is determined from the M-mode image extracted from that sequence. Each vertical line in the M mode consists of M pixels, and the horizontal line of N pixels, where N is the number of images in a sequence (each acquired at a distinct time t_n). Each pixel in the M-mode image ($M \times N$ pixels in total) is a data point, and the magnitude of each point is the intensity, denoted as $I'_{y_i}(z_m, t_n)$. Giving a candidate period T' , the phase, p_n , of each data point is

$$p_n = t_n - [t_n/T']T' \quad (n = 1, \dots, N), \quad (1)$$

where $[\cdot]$ denotes integer part. Using p_n , vertical lines in the M-mode image are resequenced by their phases such that $p_{n-1} \leq p_n \leq p_{n+1}$.

The total length, D , of the strings is

$$D^2(y_i, T') = \sum_{m=1}^M \sum_{n=2}^N [|I'_{y_i}(z_m, p_n) - I'_{y_i}(z_m, p_{n-1})|^2 + |p_n - p_{n-1}|^2 / T'^2]. \quad (2)$$

The right-hand side terms in Eq. (2) are the differences in magnitudes and in phases of two consecutive pixels in the resequenced M-mode image and are functions of T' . To give equal weights to both terms,³⁴ I'_{y_i} and p_n are normalized, such that their values lie into the range $[0, 1]$.

The cardiac period $T(y_i)$ is found by minimizing the string length $D(y_i, T')$,

$$T(y_i) = \min_{T'} D^2(y_i, T') \quad T' \subseteq [T_{\min}, T_{\max}]. \quad (3)$$

The string length $D(y_i, T')$ is a nonconvex function of T' with several local minima. Thus, searching algorithms based on

gradient methods might be trapped in local extremes,³⁷ and direct searching for T was used here within a range $[T_{\min}, T_{\max}]$.

2.2.2 Determination of relative phase shift between adjacent image sequences

To synchronize nongated image sequences, we determine the temporal relation (or phase shift) between adjacent sequences assuming structural similarity. We find the phase shift by maximizing the similarity of M-mode images—extracted along the same line ($x=x_k$) from two adjacent B-mode image sequences. Thus, we performed structural similarity along a line of the image sequences.

To improve the accuracy of the synchronization, which is limited by image acquisition rate, we pooled M-mode image data (from several cycles) into one cardiac cycle, rearranging vertical lines by their phases. The algorithms to determine phase shifts (described below) require M-mode images with the same number of vertical lines, equally spaced in time. To accomplish this, we normalized the cardiac cycle and resampled each M-mode image with the same number (K) of evenly phase-distributed vertical lines. Resampling was performed using cubic spline interpolation, which offers the best cost-performance tradeoff among available interpolation methods.^{38,39}

Structural similarity between two resampled M-mode images, $I'_i(z, p^*)$ and $I'_{i+1}(z, p^*)$, extracted from adjacent image sequences was calculated using a correlation coefficient $C_{i,i+1}$ between the M-mode images as the similarity index,

$$C_{i,i+1}(s) = \sum_{m=1}^M \sum_{n=1}^K I'_{y_i}(z_m, p_n^*) I'_{y_{i+1}}(z_m, p_n^* - s), \quad (4)$$

where s is a candidate phase shift and p^* is the phase in the normalized cardiac cycle. The phase shift, $S_{i,i+1}$, between the two adjacent image sequences is then found by maximizing the similarity index $C_{i,i+1}(s)$,

$$S_{i,i+1} = \max_s C_{i,i+1}(s) \quad s \subseteq [0, 1]. \quad (5)$$

2.2.3 Determination of absolute phase shift with respect to a reference sequence

The next step is to synchronize the image sequences with respect to a common reference sequence. Taking the first image sequence ($y_1=0$) as the reference, the absolute phase shift S_i —the phase shift between a sequence at y_i and the reference—is the accumulated sum of relative phase shifts (between adjacent image sequences),

$$S_i = \sum_{j=1}^{i-1} S_{j,(j+1)} \quad \text{with } i = 2, \dots, L \text{ and } S_1 = 0. \quad (6)$$

2.2.4 Estimation and adjustment of phase lag for all image sequences

During early developmental stages, contractile cardiac waves travel from the heart atrium to the OFT,⁴⁰ producing a peristaltic-like motion of the heart wall and introducing phase

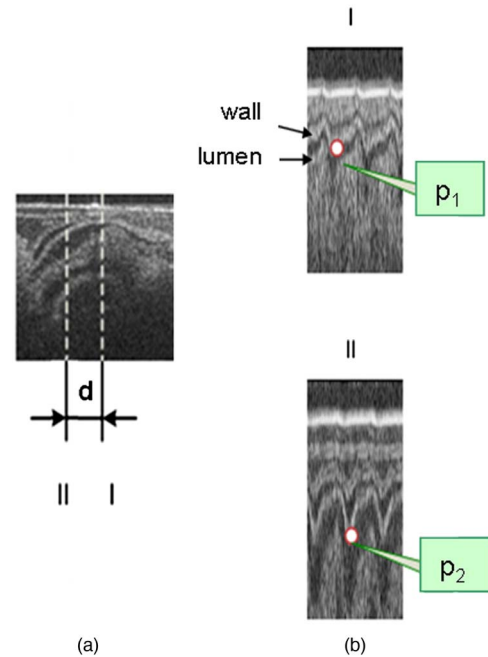


Fig. 3 Illustration of how phase lags in OFT wall motion are estimated: (a) OCT image of a longitudinal section of the OFT and (b) M-mode images extracted from the longitudinal section at the locations I (close to the OFT inlet) and II (close to the OFT outlet) in (a). Note that M-mode images were magnified and cropped for better visualization. d is the distance between locations I and II; p_1 and p_2 are the phases of maximal OFT wall contraction identified from the M-mode images extracted along lines I and II, respectively.

lags among different regions of the heart. To estimate these phase lags (p_{lag}) between adjacent image sequences, we use data from the acquired image sequence showing the longitudinal section of the heart. Two M-mode images are extracted at two locations a distance d apart along the longitudinal cardiac section (see Fig. 3). The phases of maximal cardiac contraction, p_1 and p_2 , are then identified from the M-mode images, and the phase lag, Δp , between these two locations is calculated. To minimize errors in the estimation of Δp , we average Δp over several cycles, i.e.,

$$\Delta p = \frac{1}{q} \sum_{i=1}^q (p_1^i - p_2^i), \quad (7)$$

where i represents the i 'th cardiac cycle and q is the number of sampled cardiac cycles. Assuming that the velocity of the contractile wave, v , is constant in the cardiac region under consideration,

$$v = d/\Delta p. \quad (8)$$

The phase lag between two adjacent image sequences a distance h apart is then estimated by

$$p_{\text{lag}} = h/v. \quad (9)$$

The adjusted absolute time shifts, S'_i , are then calculated by

$$S'_i = S_i + (i - 1)p_{\text{lag}}. \quad (10)$$

The assumption of constant v holds approximately true in relatively small regions of the heart (such as the OFT), and hence to achieve accurate reconstruction, phase lags should be evaluated at each individual region.

2.2.5 Reconstruction of 4-D images

To reconstruct 4-D cardiac images from a nongated data set, images in image sequences are shifted in time according to adjusted phase shifts (S'_i). We then pooled the images to a normalized cardiac cycle and resampled images at P selected equally spaced phases over the cardiac cycle, using linear interpolation between images. We then assembled 2-D images into 3-D image datasets at the P phases and reconstructed 4-D images of the heart.

3 Application to 4-D Images of the Chick Heart OFT

Our imaging strategy and synchronization procedure were used in imaging the heart OFT of chick embryos at stage HH18 (approximately three days of incubation). OFT images were acquired with OCT, and the algorithms to calculate cardiac period and phase shifts were tested for accuracy and sensitivity to the line chosen to extract M-mode images.

3.1 Embryo Preparation

Fertilized white leghorn eggs were incubated blunt-end up at 38 °C and 85% humidity in a horizontal rotation incubator to stage HH18.³² To expose the embryonic heart, the egg shell was opened and the membrane overlaying the embryo was removed. During egg manipulation and imaging, temperature of the embryo was allowed to drop below its normal physiological temperature (~ 38 °C), which allowed the heart rate to drop.

3.2 Image Acquisition with OCT

A spectral domain OCT system was used to acquire images of the OFT of a chick embryo at HH18. OCT acquired 40 B-scans (2-D image frames, see Fig. 1) per second; with each B-scan composed of 250 A-scans (line scans). The OCT system employed has ~ 10 μm axial (Z in Fig. 1) and ~ 16 μm lateral (X and Y in Fig. 1) spatial resolutions and a light penetration depth of ~ 2.0 mm in tissue (assuming a refractive index of 1.35). Because at the early developmental stages under study the chick tissue is almost transparent, light penetration depth is further limited only by blood, such that the practical penetration depth when imaging the OFT is ~ 1 mm (enough to image the OFT at HH18).

We used the nongated image acquisition strategy described in Sec. 2.1 to obtain a 4-D image data set of the OFT. A total of 65 B-mode image sequences of OFT cross sections were taken along the OFT, 12.5 μm apart, spanning the entire OFT region (~ 800 μm in length). Each image was 250 \times 430 pixels, and each image sequence consisted of 185 frames (more than five cardiac cycles). A B-mode image sequence, corresponding to a longitudinal OFT section approximately perpendicular to the center cross section of the OFT, was also acquired to adjust phase lags due to peristaltic-like wall motion in the OFT.

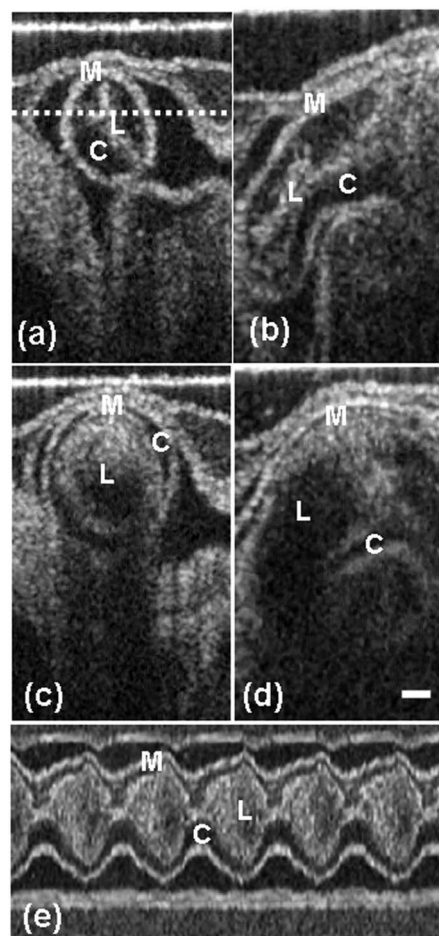


Fig. 4 Representative OCT images (in B and M modes) of the heart OFT from an HH18 chick embryo. Images show the OFT when its walls are constricted: (a) cross section of the OFT at about its center and (b) longitudinal section approximately perpendicular to the cross section in (a); and when OFT walls are expanded: (c) center cross section and (d) longitudinal section. In (c) and (d), the dark areas in the lumen are due to a transient fading of signals when image acquisition rate is lower than the speed of blood flow. (e) An M-mode image generated from the cross-sectional image sequence along the dotted line in (a). M, myocardium; C, cardiac jelly; L, lumen. Scale bar=100 μm .

Figures 4(a)–4(d) show representative OCT images of the OFT. The structure of the OFT wall—the lumen interface, cardiac jelly, and myocardium—is clearly demarcated. We extracted an M-mode image from the dotted line in Fig. 4(a). The M-mode image [Fig. 4(e)] traces the periodic displacements of the OFT wall over the acquired cardiac cycles.

3.3 Testing the Synchronization Procedure

Using the OFT images acquired with OCT, we tested the accuracy of the synchronization procedure and the sensitivity of the procedure to the line chosen to extract M-mode images. We performed most of the tests on a representative image sequence of the OFT acquired approximately at the center cross section of the OFT [see Figs. 4(a) and 4(c)].

3.3.1 Determination of cardiac period

We used the SLM algorithm, applied to M-mode images, to determine the cardiac period, T , of the chick embryonic heart from each acquired image sequence (see Sec. 2.2.1). Because during imaging embryo temperature was lower than physiological temperature (see Sec. 3.1), calculated T (~ 0.8 s, see below) was higher than normal (usually < 0.5 s for an HH18 embryo⁸). To quantify T we used Eq. (3), with a search range of cardiac periods from 0.7 to 0.9 s and searching step size of 10^{-4} s.

Accuracy. To study the accuracy of the SLM algorithm applied to M mode, we compared cardiac periods calculated using SLM applied to M- and B-mode images, as well as calculated using fast Fourier transform⁴¹ (FFT) (FFT was performed on a curve showing the correlation of the images in a sequence with respect to a reference image). To this end, we used the representative OCT image sequence of the OFT (Sec. 3.3). The cardiac period calculated using FFT ($T=0.7708$ s) was not expected to be accurate due to the small data sampling size (only approximately five cycles). The SLM algorithm, in contrast, was accurate and predicted approximately the same solution ($T=0.8146$ s) regardless of whether M- or B-mode images were used (the difference was less than the searching step). SLM applied to M-mode images, however, was >200 times faster than SLM applied to B-mode images.

To verify the accuracy of the calculated T , we pooled all the images in the sequence into one cardiac cycle, arranging them by phase according to the calculated T . From these pooled sequences, we generated M-mode images along the dotted line shown in Fig. 4(a). Figure 5 shows a comparison of M-mode images extracted from an acquired image sequence [Fig. 5(a)] and from pooled images [Figs. 5(b) and 5(c)]. The M-mode image from the acquired image sequence [Fig. 5(a)] shows a pixelated view due to the low image acquisition rate (40 fps). The M-mode image obtained from pooled images arranged according to the T calculated from FFT [Fig. 5(c)] shows that if T is inaccurate, the M-mode image looks discontinuous. The M-mode image obtained from pooled images arranged according to the T calculated using the SLM [Fig. 5(b)] is smooth looking and resembles Fig. 5(a), indicating that the T calculated using SLM is accurate.

Sensitivity to M-mode line. To test the sensitivity of the SLM algorithm to the line selected to extract the M-mode image from the 2-D image sequences, we extracted M-mode images along horizontal and vertical lines (lines were $\sim 130\text{-}\mu\text{m}$ apart, see Fig. 6) from the representative OCT image sequence. Lines were grouped according to the following criteria: (i) lines that overlay the OFT region over the cardiac cycle (H3–H5 and V3–V5); (ii) lines that overlay the OFT region only for a time interval during the cardiac cycle (V2, H2, V6, and H6); and (iii) lines that lie outside the OFT region (H1, V1, H7, and V7). We calculated T using the SLM algorithm applied to these M-mode images (see Table 1).

We found that SLM was, in general, robust, as long as the lines from which M-mode images were extracted overlaid the OFT during the cardiac cycle (i.e., H3–H5 and V3–V5); the maximum deviation from T occurred at V4 and was within 0.1%. The deviation at V4, however, was mainly due to tran-

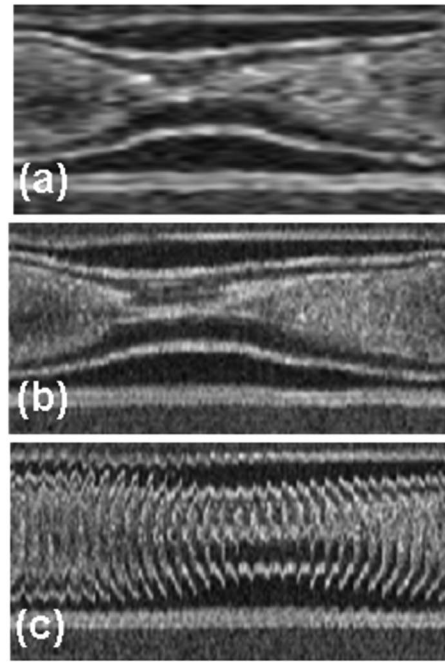


Fig. 5 M-mode images extracted from cross-sectional image sequences of the OFT along the dotted line in Fig. 4(a). Shown M-mode images were extracted from (a) the acquired OCT image sequence, (b) the same OCT image sequence pooled to one cycle using the cardiac period calculated by SLM ($T=0.8146$ s), and (c) the same sequence pooled to one cycle using the cardiac period calculated by FFT ($T=0.7708$ s). Note that (a) corresponds to one cardiac cycle of Fig. 4(e).

sient fading of signals during imaging (wash-out phenomenon),⁴² which occurs when blood flow velocity is much faster than image acquisition rates, resulting in interference signals that average out and appear as a dark region in the lumen [see Figs. 4(c) and 4(d)]. Better reproducibility of results was achieved when SLM was applied to M-mode images extracted from horizontal rather than vertical lines. The inferior performance of the M-mode images from vertical lines was due to both attenuation of signals along the tissue depth and transient fading of signals.

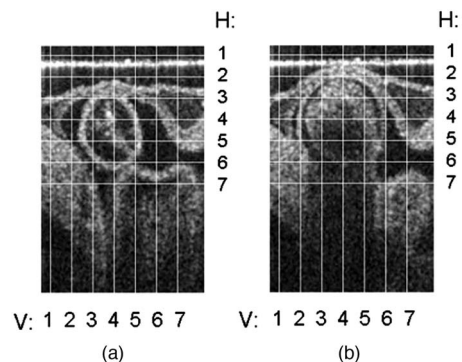


Fig. 6 Lines chosen to perform sensitivity study in determining cardiac periods using SLM algorithm applied to M-mode (from the representative sequence shown in Fig. 4). The panels show the positions of the lines when the OFT walls were most (a) constricted and (b) expanded.

Table 1 Cardiac periods (in seconds) calculated from M-mode images extracted from different lines (see Fig. 6).

	1	2	3	4	5	6	7
H	0.8180	0.8146	0.8146	0.8146	0.8146	0.8206	0.8146
V	0.8206	0.8146	0.8146	0.8153	0.8146	0.8146	0.8125

Bold numbers show calculated periods that are within 0.01% accuracy with respect to the centerline [shown in Fig. 4(a)] used to determine the accuracy of SLM.

3.3.2 Determination of relative phase shift

To calculate phase shifts, $S_{i,i+1}$, between adjacent image sequences, we used a similarity algorithm that searched for $S_{i,i+1}$ by maximizing the correlation between M-mode images [Eq. (5)]. Because each image sequence consisted of 185 frames, $S_{i,i+1}$ was expected to be at least accurate within one frame in a pooled sequence (or $\sim 0.005T$).

Accuracy. To study the accuracy of the similarity algorithm applied to M-mode images, we first tested the algorithm using synthetically generated image sequences with known relative phase shifts. To obtain the image sequences, we chose the representative image sequence [see Fig. 4(a) and 4(c)] and, using linear interpolation between frames, we then generated 10 image sequences that were shifted in phase from the representative sequence. Phase shifts were randomly chosen from 0 to T . Using these sequences, we compared the performance of the similarity algorithms applied to B- and M-mode images [extracted along the line shown in Fig. 4(a)] in terms of accuracy and computational efficiency.

We found small errors—with respect to known shifts (maximum $\sim 0.3\%$)—when phase shifts were calculated using similarity on either B- or M-mode images. Calculation of the phase shift using M-mode images, however, was ~ 400 times faster than when using B-mode images.

Sensitivity to M-mode line. To study the sensitivity of calculated phase shifts to the line selected to extract the M-mode images, we used the representative image sequence [see Fig. 4(a) and 4(c)] together with its adjacent image sequence, and applied the similarity algorithm to M-mode images extracted from the two image sequences. According to Sec. 3.3.1, T was more accurate when lines that overlaid the OFT over the cardiac cycle were used to extract M-mode images; therefore, we focused on M-mode images extracted from these lines. We generated 16 M-mode images extracted from horizontal and vertical lines ($50\text{-}\mu\text{m}$ apart, see Fig. 7), and found the phase shift between the sequences by applying similarity, Eq. (5), to these M-mode images. Calculated phase shifts, $S_{i,i+1} = (0.25 \pm 0.005)T$, for all M-mode lines were within the expected accuracy.

3.3.3 Reconstruction of 4-D images of the OFT

To reconstruct 4-D images of the OFT, we used the 4-D data set obtained as described in Sec. 3.2. For each OFT cross-sectional image sequence, we generated an M-mode image from a horizontal line within the center region of the OFT cross section (e.g., line H4 in Fig. 6). Then, using the SLM algorithm [Eqs. (2) and (3)], we determined T for each image

sequence. Once T was determined, we used similarity [Eqs. (4) and (5)], to determine the relative phase shift between each adjacent image sequence pair. Finally, we estimated the phase lag among image sequences due to the peristaltic-like motion of the OFT wall [Eqs. (8) and (9)] from the acquired sequence of OFT longitudinal section images. This phase lag was found to be $\sim 0.32T$ from the inlet to the outlet of the OFT, and thus was non-negligible. After calculating absolute phase shifts with respect to a reference sequence [Eq. (6)], we corrected for this phase lag [Eq. (10)], and then synchronized image sequences according to the adjusted absolute phase shifts. We then reassembled the 2-D images of the OFT into 3-D image data sets at 180 phases of the cardiac cycle, and thus reconstructed 4-D images of the OFT. To better visualize the structure and motion of the OFT walls and their interaction with blood flow over the cardiac cycle, 4-D images were further analyzed using the image software Amira 3.1 (see Video 1).

Accuracy. To test the accuracy of the 4-D reconstruction, we extracted image sequences showing an OFT longitudinal section over the cardiac cycle from the reconstructed 4-D images with and without phase-lag adjustment. By visual inspection, the plane at which OFT longitudinal sections were extracted from reconstructed images was close to the plane where the OFT longitudinal image sequence was acquired directly with OCT. We then extracted M-mode images from three lines of the reconstructed and imaged OFT longitudinal sections (see Fig. 8): (i) line I, which was close to the ventricle (the OFT inlet); (ii) line M, approximately at the middle of the OFT; and (iii) line O, which was close to the aortic sac (the OFT outlet). The extracted M-mode images showed very similar

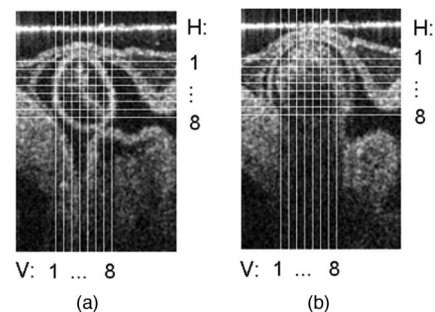
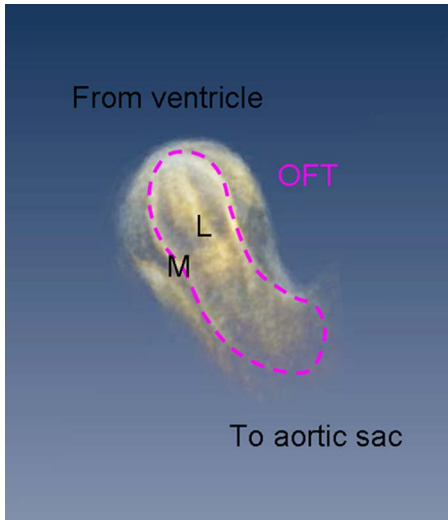


Fig. 7 Lines chosen to perform sensitivity study in determining relative phase shifts using similarity algorithms applied to M-mode images (from the representative sequence shown in Fig. 4). The panels show the positions of the lines when the OFT walls were most (a) constricted and (b) expanded.



Video 1 Voxel view of a beating chick-embryo OFT. The movie shows a frontal view of the OFT for the first cardiac cycle and then a 180-deg rotation of the OFT along the Z-axis for the second cardiac cycle. The dotted line (in the still image) encircles the OFT region that connects the ventricle proximally and aortic sac distally. M: myocardium, L: lumen (Quick-Time, 2 MB). [URL: <http://dx.doi.org/10.1117/1.3184462.1>]

wall-motion patterns. To better visualize differences in wall-motion phase relations, we manually traced the upper interface between the myocardium and the cardiac jelly from the M-mode images and plotted the displacement of this interface over time (see Fig. 9). We found that when the OFT is recon-

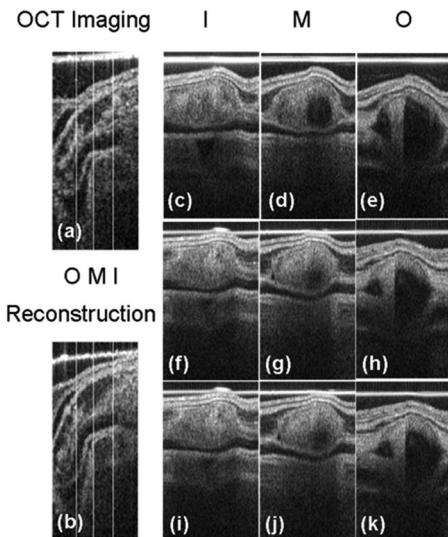


Fig. 8 Comparison of M-mode images extracted from imaged and reconstructed longitudinal sections of the OFT. Lines selected to extract M-mode images are shown in (a) and (b): close to the OFT inlet (I), middle OFT (M), and close to the outlet (O). (a) Longitudinal sections acquired directly with OCT and (b) reconstructed from synchronized 4-D image data. (c–e) M-mode images from a sequence acquired directly from OCT; (f–h) M-mode images from a reconstructed image sequence without phase lag adjustment; (i–k) M-mode images from the reconstructed image sequence with phase lag adjustment.

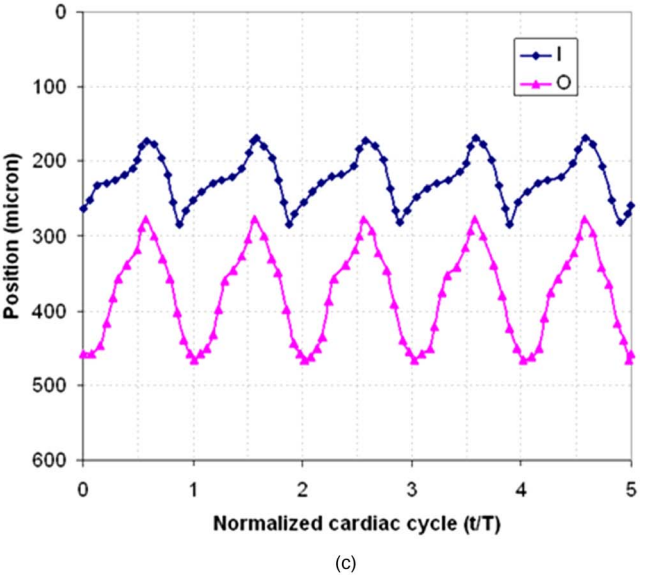
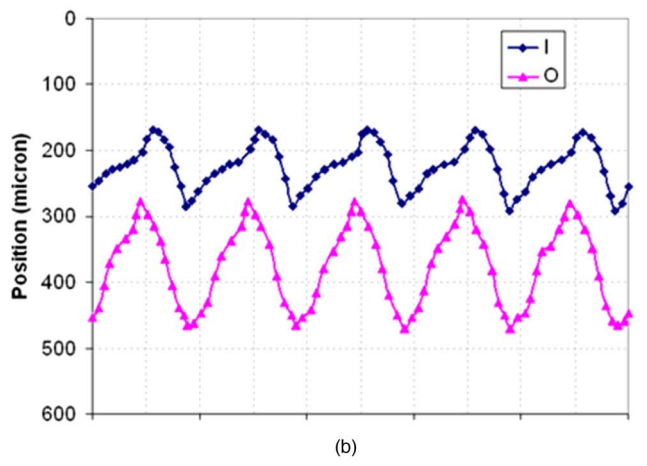
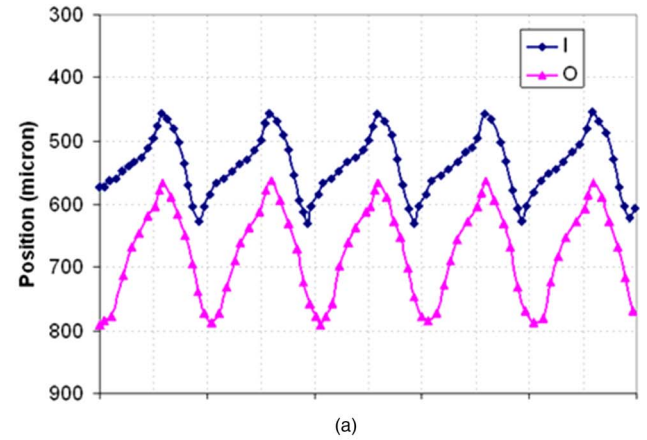


Fig. 9 OFT wall displacements close to the inlet and outlet. Wall displacements (showing the motion of the interface between the myocardium and cardiac jelly) were traced manually from the M-mode images shown in Fig. 8: (a) from images acquired directly with OCT [Figs. 8(c) and 8(e)]; (b) from reconstructed images without phase adjustment [Figs. 8(f) and 8(h)]; and (c) from reconstructed images with phase adjustment [Figs. 8(i) and 8(k)]. For ease of visualization, we present five cardiac cycles extracted directly from the acquired image sequence (a), and in (b) and (c) generated by circular repetition of the reconstructed pooled cardiac cycle.

structed without phase-lag adjustment, phase relations between lines I and O— $(0.02 \pm 0.02)T$ —did not resemble those observed from direct OCT imaging— $(0.11 \pm 0.02)T$. When phase-lag adjustment was introduced in the reconstruction, however, the phase relations between lines I and O were recovered. Thus, our results indicate that phase-lag adjustment is needed to properly capture the dynamics of the OFT wall motion.

4 Discussions

In this paper, we present an imaging strategy together with an accurate and efficient postacquisition synchronization procedure to assemble nongated 2-D cardiac image sequences (B-mode images) into a synchronized 4-D image data set. Phase shifts between adjacent image sequences are calculated by maximizing the similarity of M-mode images extracted from B-mode images. In the proposed procedure, the M-mode images function as an optical cardiogram, providing gating data used for postacquisition synchronization.²⁷ Furthermore, our synchronization procedure provides a means of estimating phase lags in the motion of cardiac walls, introduced for instance by peristaltic-like wall contractions, and adjusting phase lags for proper image reconstruction. Because synchronization of image sequences is performed using line scans (M-mode images), computational efficiency is achieved.

4.1 Application Realm of the Synchronization Procedure

Application of our procedure to 4-D image reconstruction is subjected to two underlying assumptions. The first assumption is the periodicity of cardiac motion and deformation. For chick embryos at early developmental stages, the central neural system, which regulates heart rate, has not yet developed and the heart rate is only a function of embryo temperature. Although during our imaging acquisition the temperature of the embryo was lower than physiological, temperature was stable within 1 °C and temperature-induced variations in the heart rate were small (<9% among image sequences). Thus, during imaging, motion of the OFT wall was approximately periodic. The second assumption is structural similarity of image sequences acquired at adjacent locations. To ensure structural similarity, the distance h (12.5 μm) between acquired cross-sectional image sequences was less than the lateral spatial resolution of our OCT system (16 μm), and much smaller than the length of the OFT ($\sim 800 \mu\text{m}$). Our nongated 4-D imaging strategy and synchronization procedure can be generalized to applications involving other animal models or organ systems, as well as other imaging modalities.

4.2 Accuracy of the Synchronization Procedure

The accuracy of our synchronization procedure depends on the line chosen to extract M-mode images from B-mode images. We found that calculations of period and relative phase shift from M-mode images are not too sensitive to the locations or orientations of the lines as long as the lines overlaid the region of interest (e.g., the OFT) over the entire cardiac cycle. For OCT images, however, attenuation of the imaging signal along the tissue depth and the transient fading of signal due to fast motion of blood flow affect the accuracy of calcu-

lations. Therefore, lines containing points within the same depth in tissue (horizontal lines in Figs. 6 and 7) and within the center region of the OFT are preferred.

OCT images of the OFT (B and M modes) contain periodic data from the OFT (our region of interest), but also data from other parts of the heart and surrounding organs, such as the head. To estimate the percentage of the image that contains OFT (useful) data, we can use the average surface of the image occupied by the OFT over total surface area for B-mode images, and the average OFT length over total line length for M-mode images. For cross-sectional images, we can assume that the OFT external layer is a circle with radius R , and that the image is a square with side length L (with $R < L$). Then, the ratio of OFT data to total imaging data goes as $(R/L)^2$ for 2-D images and R/L for line scans. Because $R/L > (R/L)^2$, using properly chosen lines for M-mode extraction, the algorithms to calculate period and phase shift could achieve higher accuracy when applied to M-mode rather than B-mode images.

We compared the performance of the algorithms used to calculate cardiac period and relative phase shifts applied to B- and M-mode images obtained from a horizontal line within the center region of the OFT (see Figs. 6 and 7). We found that, regardless of whether the algorithms were applied to B- or M-mode images, similar accuracy was achieved (see Secs. 3.3.1 and 3.3.2). Moreover, calculations were significantly faster (~ 400 times faster) when performed using M-mode rather than B-mode images. Employing M-mode images dramatically improved the efficiency of the synchronization procedure without compromising accuracy.

Other factors that affect accuracy of our synchronization procedure are the number of frames per cardiac cycle that the system can acquire and the total number of cardiac cycles acquired in a sequence. Our reconstruction is based on ~ 30 frames per cycle and ~ 5 cardiac cycles, thus about 150 frames in total to accurately reconstruct a cardiac cycle (as all the images are pooled to one cycle). We verified that this number of frames is sufficient for correct reconstruction. We also checked the accuracy of the reconstruction if more or less frames were considered (results not shown in the manuscript) and our results suggest that 150 frames are probably close to optimal. Thus, for other systems and faster cardiac rates, image acquisition should be such that at least 150 frames are acquired. A caveat, however, is that if the number of frames acquired per cardiac cycle is $\ll 30$, then each image frame might not be considered “instantaneous” (because it takes time for the system to scan the frame) and this would introduce inaccuracies. Our results indicate that acquiring OCT images at a rate of ~ 30 frames/cardiac cycle for about five cardiac cycles is sufficient to predict cardiac cycle and time shifts with reasonable accuracy.

4.3 4-D Reconstruction (Phase-Lag Correction)

We found that synchronization of images based on structural similarity alone is not sufficient to capture the peristaltic-like motion of the heart walls of chick embryos at early developmental stages. During early development, the embryonic heart does not have valves and, to maintain unidirectional blood flow, contractile waves travel along the heart.⁴⁰ These traveling waves produce peristaltic-like wall motion and thus intro-

duce phase lags between different regions of the heart. In our synchronization procedure, to correctly recover the dynamics of the OFT wall, we adjusted the phases of image sequences from those obtained by structural similarity.

Because contractile waves travel from the inlet to the outlet of the heart, the need to correct for the phase lag in our procedure largely depends on our choice of imaging cross-sectional (transverse) planes. For our procedure, we acquired cross-sectional images because they ensure similarity between adjacent image sequences (i.e., the OFT always shows in the image frame, no matter whether the OFT is expanded or contracted), whereas with longitudinal images, there are imaging planes from which the OFT “disappears” when its walls contract and “reappears” when its walls expand, making similarity algorithms more difficult to implement and more prone to inaccuracies.

Currently, there is controversy about the nature of cardiac motion at early stages of development, with some authors arguing that heart wall motion is peristaltic,^{43,44} whereas others argue that the heart acts as a suction pump.⁴⁵ We certainly found that in reconstructing the OFT motion from the nongated OCT images we acquired, phase-lags in wall motion between the inlet and outlet of the OFT (not accounted for by structural similarity) need to be considered. In other regions of the heart, and/or at later stages, this phase lag might be negligible. Application of our synchronization procedure, however, will certainly aid in the characterization of cardiac mechanics during early development.

5 Conclusions

In this paper, we have presented a 4-D nongated imaging strategy and postacquisition synchronization procedure to reconstruct 4-D images of the embryonic heart. We have demonstrated the efficiency and accuracy of the procedures by reconstructing the cardiac OFT of a chick embryo from OCT images. Our nongated 4-D imaging strategy and synchronization procedure can be generalized to applications involving other animal models or organ systems, as well as other imaging modalities, providing that the two underlying assumptions, periodicity of the motion and similarity of adjacent image sequences, are satisfied. The synchronization procedure presented is especially useful for 4-D imaging when: (i) reliable physiological gating signals are difficult to acquire, (ii) the acquisition rate of the imaging system employed is limited, and (iii) phase lags are non-negligible.

Acknowledgments

This work was supported, in part, by a Beginning Grant-in-Aid from the Pacific Mountain Affiliate of the American Heart Association (Grant No. 0760063Z). The authors are grateful to Dr. Sandra Oster for her editorial assistance.

References

1. A. F. M. Moorman and V. M. Christoffels, “Cardiac chamber formation: Development, genes, and evolution,” *Physiol. Rev.* **83**(4), 1223–1267 (2003).
2. E. N. Olson, “A decade of discoveries in cardiac biology,” *Nat. Med.* **10**(5), 467–474 (2004).
3. T. Bartman and J. Hove, “Mechanics and function in heart morphogenesis,” *Dev. Dyn.* **233**(2), 373–381 (2005).
4. E. B. Clark and G. C. Rosenquist, “Spectrum of cardiovascular

- anomalies following cardiac loop constriction in the chick embryo,” *Birth Defects Orig Artic Ser.* **XIV**(7), 431–442 (1978).
5. J. Bartman, E. C. Walsh, K. K. Wen, M. McKane, J. H. Ren, J. Alexander, P. A. Rubenstein, and D. Y. R. Stainier, “Early myocardial function affects endocardial cushion development in zebrafish,” *PLoS Biol.* **2**(5), 673–681 (2004).
6. J. R. Hove, R. W. Koster, A. S. Forouhar, G. Acevedo-Bolton, S. E. Fraser, and M. Gharib, “Intracardiac fluid forces are an essential epigenetic factor for embryonic cardiogenesis,” *Nature (London)* **421**(6919), 172–177 (2003).
7. J. Männer, “Cardiac looping in the chick embryo: A morphological review with special reference to terminological and biomechanical aspects of the looping process,” *Anat. Rec.* **259**(3), 248–262 (2000).
8. N. Hu and E. B. Clark, “Hemodynamics of the stage 12 to stage 29 chick embryo,” *Circ. Res.* **65**, 1665–1670 (1989).
9. J. M. Schmitt, “Optical coherence tomography (OCT): a review,” *IEEE J. Sel. Top. Quantum Electron.* **5**(4), 1205–1215 (1999).
10. S. A. Boppart, “Optical coherence tomography—principles applications and advances,” *Minerva Biotechnol.* **16**(4), 211–237 (2004).
11. J. G. Fujimoto, “Optical coherence tomography for ultrahigh resolution *in vivo* imaging,” *Nat. Biotechnol.* **21**(11), 1361–1367 (2003).
12. P. H. Tomlins and R. K. Wang, “Theory, developments and applications of optical coherence tomography,” *J. Phys. D* **38**(15), 2519–2535 (2005).
13. M. Liebling, A. S. Forouhar, R. Wolleschensky, B. Zimmermann, R. Ankerhold, S. E. Fraser, M. Gharib, and M. E. Dickinson, “Rapid three-dimensional imaging and analysis of the beating embryonic heart reveals functional changes during development,” *Dev. Dyn.* **235**(11), 2940–2948 (2006).
14. K. Tobita, J. B. Garrison, L. J. Liu, J. P. Tinney, and B. B. Keller, “Three-dimensional myofiber architecture of the embryonic left ventricle during normal development and altered mechanical loads,” *Anat. Rec. Suppl.* **283A**(1), 193–201 (2005).
15. C. K. L. Phoon, “Imaging tools for the developmental biologist: ultrasound biomicroscopy of mouse embryonic development,” *Pediatr. Res.* **60**(1), 14–21 (2006).
16. M. W. Jenkins, F. Rothenberg, D. Roy, V. P. Nikolski, Z. Hu, M. Watanabe, D. L. Wilson, I. R. Efimov, and A. M. Rollins, “4-D embryonic cardiography using gated optical coherence tomography,” *Opt. Express* **14**(2), 736–748 (2006).
17. S. A. Boppart, M. E. Brezinski, and J. G. Fujimoto, “Optical coherence tomography imaging in developmental biology,” *Methods Mol. Biol.* **135**, 217–233 (2000).
18. T. M. Yelbuz, M. A. Choma, L. Thrane, M. L. Kirby, and J. A. Izatt, “Optical coherence tomography—a new high-resolution imaging technology to study cardiac development in chick embryos,” *Circulation* **106**(22), 2771–2774 (2002).
19. E. A. Swanson, M. R. Hee, G. J. Tearney, B. Boumar, S. Boppart, J. Izatt, M. E. Brezinski, J. S. Schuman, and C. A. Puliafito, “Optical coherence tomography principles, instrumentation, and biological applications,” *Biomedical Optical Instrumentation and Laser-Assisted Biotechnology*, A. M. Scheggi, S. Martellucci, A. N. Chester, and R. Pratesi, Eds. 291–303, Springer, New York (1996).
20. R. Yelin, D. Yelin, W.-Y. Oh, S. H. Yun, C. Boudoux, B. J. Vakoc, B. E. Bouma, and G. J. Tearney, “Multimodality optical imaging of embryonic heart microstructure,” *J. Biomed. Opt.* **12**(6), 064021 (2007).
21. J. Männer, L. Thrane, K. Norozi, and T. M. Yelbuz, “High-resolution *in vivo* imaging of the cross-sectional deformations of contracting embryonic heart loops using optical coherence tomography,” *Dev. Dyn.* **237**(4), 953–961 (2008).
22. S. Rugonyi, C. Shaut, A. Liu, K. Thornburg, and R. K. Wang, “Changes in wall motion and blood flow in the outflow tract of chick embryonic hearts observed with optical coherence tomography after outflow tract banding and vitelline-vein ligation,” *Phys. Med. Biol.* **53**(18), 5077–5091 (2008).
23. W. Luo, D. L. Marks, T. S. Ralston, and S. A. Boppart, “Three-dimensional optical coherence tomography of the embryonic murine cardiovascular system,” *J. Biomed. Opt.* **11**(2), 021014 (2006).
24. M. W. Jenkins, D. C. Adler, M. Gargasha, R. Huber, F. Rothenberg, J. Belding, M. Watanabe, D. L. Wilson, J. G. Fujimoto, and A. M. Rollins, “Ultrahigh-speed optical coherence tomography imaging and visualization of the embryonic avian heart using a buffered Fourier domain mode locked laser,” *Opt. Express* **15**(10), 6251–6267 (2007).
25. W. G. O’Dell and A. D. McCulloch, “Imaging three-dimensional car-

- diac function," *Annu. Rev. Biomed. Eng.* **2**, 431–456 (2000).
26. M. W. Jenkins, O. Q. Chughtai, A. N. Basavanahally, M. Watanabe, and A. M. Rollins, "In vivo gated 4-D imaging of the embryonic heart using optical coherence tomography," *J. Biomed. Opt.* **12**(3), 030505 (2007).
 27. A. Mariampillai, B. A. Standish, N. R. Munce, C. Randall, G. Liu, J. Y. Jiang, A. E. Cable, I. A. Vitkin, and V. X. D. Yang, "Doppler optical cardiogram gated 2-D color flow imaging at 1000 fps and 4-D in vivo visualization of embryonic heart at 45 fps on a swept source oct system," *Opt. Express* **15**(4), 1627–1638 (2007).
 28. M. Liebling, A. Forouhar, M. Gharib, S. Fraser, and M. Dickinson, "Four-dimensional cardiac imaging in living embryos via postacquisition synchronization of nongated slice sequences," *J. Biomed. Opt.* **10**(5), 054001 (2005).
 29. M. Liebling, A. S. Forouhar, M. Gharib, S. E. Fraser, and M. E. Dickinson, "Wavelet-based synchronization of nongated confocal microscopy data for 4-D imaging of the embryonic heart," *Proc. SPIE* **5914**, 591409 (2005).
 30. S. Carerj, A. Micari, A. Trono, G. Giordano, M. Cerrito, C. Zito, F. Luzzza, S. Coglitore, F. Arrigo, and G. Oreto, "Anatomical M-mode: an old-new technique," *Echocardiogr.* **20**(4), 357–361 (2003).
 31. K. Ruijtenbeek, J. G. R. De Mey, C. E. Blanco, and H. Ehmke, "The chicken embryo in developmental physiology of the cardiovascular system: a traditional model with new possibilities," *Am. J. Physiol. Regulatory Integrative Comp. Physiol.* **283**(2), R549–551 (2002).
 32. V. Hamburger and H. L. Hamilton, "A series of normal stages in the development of the chick embryo," *J. Morphol.* **88**(1), 49–92 (1951).
 33. A. C. Gittenberger-de Groot, M. M. Bartelings, M. C. Deruiter, and R. E. Poelmann, "Basics of cardiac development for the understanding of congenital heart malformations," *Pediatr. Res.* **57**(2), 169–176 (2005).
 34. M. M. Dworetzky, "A period-finding method for sparse randomly spaced observations or 'how long is a piece of string?'," *Mon. Not. R. Astron. Soc.* **203**, 917–924 (1983).
 35. R. F. Stellingwerf, "Period determination using phase dispersion minimization," *Astrophys. J.* **224**, 953–960 (1978).
 36. D. H. Roberts, J. Lehar, and J. W. Dreher, "Time series analysis with clean. I. Derivation of a spectrum," *Astron. J.* **93**(4), 968–989 (1987).
 37. R. Horst, P. M. Pardalos, and N. V. Thoai, *Introduction to Global Optimization (Nonconvex Optimization and Its Applications)*, 2nd ed., Vol. 48, Kluwer, Dordrecht (2000).
 38. E. H. W. Meijering, W. J. Niessen, and M. A. Viergever, "Quantitative evaluation of convolution-based methods for medical image interpolation," *Med. Image Anal.* **5**, 111–126 (2001).
 39. M. Unser, "Splines: a perfect fit for signal and image processing" *IEEE Signal Process. Mag.* **16**(6), 22–38 (1999).
 40. F. D. Jong, T. Ophof, A. A. M. Wilde, M. J. Janse, and R. Charles, "Persisting zones of slow impulse conduction in developing chicken hearts," *Circulation* **71**, 240–250 (1992).
 41. M. Pagani, F. Lombardi, S. Guzzetti, O. Rimoldi, R. Furlan, P. Pizzinelli, G. Sandrone, G. Malfatto, S. Dell'Orto, and E. Piccaluga, "Power spectral analysis of heart rate and arterial pressure variabilities as a marker of sympatho-vagal interaction in man and conscious dog," *Circulation* **59**(2), 178–193 (1986).
 42. W. Yimin, A. B. Bradley, A. I. Joseph, T. Ou, and H. David, "Retinal blood flow measurement by circumpapillary Fourier domain Doppler optical coherence tomography," *J. Biomed. Opt.* **13**(6), 064003 (2008).
 43. L. Taber, J. Zhang, and R. Perucchio, "Computational model for the transition from peristaltic to pulsatile flow in the embryonic heart tube," *J. Biomech. Eng.* **129**, 441–449 (2007).
 44. M. Fishman and K. Chien, "Fashioning the vertebrate heart: Earliest embryonic decisions," *Development* **124**(11), 2099–2117 (1997).
 45. A. S. Forouhar, M. Liebling, A. Hickerson, A. Nasiraei-Moghaddam, H. J. Tsai, J. R. Hove, S. E. Fraser, M. E. Dickinson, and M. Gharib, "The embryonic vertebrate heart tube is a dynamic suction pump," *Science* **312**(5774), 751–753 (2006).